Accepted Manuscript

Effect of Quality Control Parameter Variations on the Fatigue Performance of Aluminum Friction Stir Welded Joints

Shihui Guo, Luqman Shah, Rakesh Ranjan, Scott Walbridge, Adrian Gerlich

PII: S0142-1123(18)30536-X
DOI: https://doi.org/10.1016/j.ijfatigue.2018.09.004
Reference: JIJF 4839

To appear in: *International Journal of Fatigue*

Received Date: 26 April 2018
Revised Date: 22 August 2018
Accepted Date: 15 September 2018

Please cite this article as: Guo, S., Shah, L., Ranjan, R., Walbridge, S., Gerlich, A., Effect of Quality Control Parameter Variations on the Fatigue Performance of Aluminum Friction Stir Welded Joints, *International Journal of Fatigue* (2018), doi: https://doi.org/10.1016/j.ijfatigue.2018.09.004

Effect of Quality Control Parameter Variations on the Fatigue Performance of Aluminum Friction Stir Welded Joints

Shihui Guo, Luqman Shah, Rakesh Ranjan, Scott Walbridge*, Adrian Gerlich

Department of Civil and Environmental Engineering, University of Waterloo, Waterloo, ON, Canada

* Corresponding author, Email: swalbrid@uwaterloo.ca, Phone: (519) 888-4567 x38066

Abstract

This paper describes fatigue tests performed on 6061-T651 and 5083-H321 aluminum friction stir welded joints with dimensions and loading conditions typical for structural applications. Butt and lap joint details with various defects intentionally introduced were tested under tension-only constant and variable amplitude loading conditions. In this paper, the fatigue test results are presented along with supporting metallurgical and nonlinear fracture mechanics analyses. Based on this work, it is concluded that kissing bond defects on the order of 0.3-1.0 mm can result in a significant fatigue life reduction and a shift in the failure mode to the weld root. The investigated toe-flash defect had less of an effect on fatigue performance. The lap joint did not perform as well as the butt joint detail.

Keywords: Aluminum; Friction stir welds; Defects; Fracture mechanics; Variable amplitude loading

1. Introduction and Background

Friction stir welding (FSW) is a solid-state joining process. It involves rotating a cylindrical tool with a short protrusion or “pin”, which is plunged between two metal plates. High pressure and shear strain plastically deform and consolidate the work pieces by means of material extrusion from the front to the back of the tool [1]. The plates are clamped with a sturdy fixture to the backing plate with an anvil piece of hardened steel underneath the path of the FSW tool, counteracting the vertical and horizontal forces

arising during welding. The combination of frictional and deformation heating around the immersed rotating pin and at the interface between the shoulder of tool and the plates leads to the consolidation of the two metal plates as the tool traverses along the joint line [2]. FSW was invented in the Welding Institute (TWI) in the UK in 1991 by Wayne Thomas and has been researched extensively since then and applied in various fields such as the automotive, marine, and aerospace industries, where aluminum alloys are heavily used [3]. Interest in FSW for emerging applications such as vehicular bridge decks is growing due to the high productivity associated with welding thick aluminum sections in a single pass with much lower distortion compared to arc welding [4]. Due to its simple concept and operation, it has replaced fusion welding in some areas, particularly where aluminum alloys are joined. Another benefit of FSW is the solid-state process itself, which allows one to avoid reaching the liquidus temperature of the work piece, and thus prevents several detrimental defects often associated with fusion welding such as porosity, liquation cracking, and solidification cracking [5]. Other advantages include avoiding fume generation, eliminating the need for filler metal, and minimal required operator skill.

Recent efforts to introduce FSW in structural welding codes have resulted in some success. ISO and AWS standards now exist, containing provisions for the quality control and pre-qualification of FSW joints [6,7]. The Canadian code for welding of aluminum structures, CAN/CSA W59.2 [8], is presently considering the adoption of similar provisions. Generally absent in these welding standards are details concerning fatigue design. The common practice is to use the available fusion weld design curves for similar joint geometries (e.g. butt joints) in structural aluminum standards such as Eurocode 9, the Aluminum Design Manual (ADM), and CAN/CSA S157 [9-11]. Several studies have suggested that this approach may actually be overly conservative due to the improved properties of FSW versus fusion joints [12-14]. For example, it has been reported that 5xxx and 6xxx FSW samples that contained "kissing bond" defects up to 0.35 mm, cause no measurable degradation in mechanical performance

compared to defect-free welds [12]. In addition, samples with kissing bond defects up to 1 mm in depth could still meet the requirements of Eurocode 9 according to another recent study [13]. A recent state-of-the-art review presents available fatigue data for structural aluminum welds including 322 data points for a range of alloys and plate thicknesses [14]. Based on a statistical analysis of this data, the conservativism of the Eurocode and ADM design curves for fusion welded butt joints is highlighted, and a FAT62 design curve is recommended with a slope of $m = 7.0$. Recent research has investigated other issues related to the fatigue performance of FSW joints including: fatigue testing and fracture mechanics analysis of other joint details, such as "clinch joints" [15], micro-structural modelling of fatigue behaviour [16,17], and FSW joints in other alloys [18] and dissimilar alloys [19].

Despite this recent progress, a number of gaps in the current state-of-the-knowledge appear to remain unaddressed [14]. In addition to the conservative fatigue performance assumptions made in the structural design codes, the tolerance limits on the various defect types in the welding codes do not appear to have been related to fatigue performance, but seem to have been established based on "best practice". A lack of fatigue data under variable amplitude loading, is also apparent.

Against this background, a study was undertaken with the following objectives:

1) to fabricate FSW joint specimens with different defect types and degrees of severity due to variations in the welding process, and to characterize the metallurgical properties of the joints using various destructive and non-destructive evaluation (NDE) methods;
2) to perform fatigue tests on the fabricated FSW joint specimens, under a range of loading conditions, including constant amplitude (CA) loading and variable amplitude (VA) loading simulating service conditions typical for vehicular bridge decks; and

3) to relate the weld quality and fatigue performance with the goal of providing recommendations for the future development of "performance-based" quality control (QC) criteria and improved fatigue design provisions for FSW joints structural aluminum applications.

So far this research has focused on two alloys: 6061-T651 and 5083-H321 and two joint geometries (butt joints and a lap joint detail) in ~10 mm thick plate. It has also focused on a limited subset of defects, including: kissing bond, toe flash (due to excessive tool penetration), and wormhole defects. This paper presents the results of the research completed to date to address the identified research needs.

2. Fatigue Test Description

The specimens tested in this study were fabricated from 6061-T651 and 5083-H321 aluminum alloy plate with nominal thicknesses of 9.5 mm and 9.1 mm, respectively. The slight variation in the nominal plate thicknesses between the specimens fabricated with these two alloys, while not preferred, was the result of local material availability. The alloy compositions were verified in accordance to ASTM Standards E1097-12 and E1479-99 [20,21] by an external laboratory (see Table 1). To fabricate the specimens, pairs of 175 mm by 420 mm plates were prepared and welded along the long edge, which was oriented parallel to the rolling direction of the plate. The welding edges were cleaned before welding to avoid contamination potentially leading to voids and unexpected defects. The plates were held in place using clamps mounting on the backing plate with both vertical and horizontal forces (see Figure 1(A)). Each of the welded plates was then cut into four "dog-bone" fatigue specimens using a CNC machine. Scrap material between each fatigue specimen was saved for subsequent metallurgical analysis. The specimens had a 90 mm width in the grip regions (see Figure 1(B)), a 70 mm minimum width in the narrow region between the grips, and a curved transition with a radius of 85 mm. A linear elastic finite element analysis verified that this geometry resulted in a stress at the weld location that was not less than the stress in the transition region adjacent to the grips.

Table 1. Compositions of base materials in weight percentage (wt%).

Elements	Al	Mn	Mg	Si	Cr	Cu	Zn	Fe
6061-T651	Balance	0.08	0.81	0.53	0.06	0.18	0.01	0.19
5083-H321	Balance	0.79	4.74	0.05	0.06	0.07	0.14	0.21

Figure 1: Specimen fabrication and loading details: (A) welding process setup, (B) specimen layout, (C) FSW tool, and (D) tested VA loading history.

For most of the specimens, the welding resulted in a butt joint between the plates. In addition to the butt joint specimens, a special lap joint detail was also investigated, which simulates a lap joint between extrusions in (for example) a multi-extrusion vehicular bridge deck panel. The lap joint is a convenient way to provide built in backing material for a one sided weld. On the other hand, it results in a crack-like gap, which runs parallel to the loading direction. One of the objectives of testing this detail was to assess the performance of this complex joint type. The lap joint specimens were fabricated by milling 19.05 mm (3/4") 6061-T651 aluminum plates to half of their thickness at one end with a filleted transition in the weld region. A profile of the lap joint detail is shown in Figure 2.

Figure 2: Specimen profiles: (A) 6061 proper weld profile, (B) 6061 toe flash / undercut weld profile, (C) lap joint detail, and (D) lap joint weld profile.

In total, six specimen types were fabricated: i) "properly welded" 6061 butt joints, ii) 6061 butt joints with kissing bond defects, iii) 6061 butt joints with toe flash defects, iv) 6061 lap joints, v) "properly welded" 5083 butt joints, and vi) 5083 butt joints with wormhole defects. The idea of testing intentionally introduced defects in this manner was similarly employed in [22] to study the effects of kissing bond defects on the behaviour of 7475 alloy FSW specimens.

The employed FSW tool was made from H13 steel, quenched and tempered to 46-48 HRC. The pin geometry is 10° tapered and M6-threaded with three flats (see Figure 1(C)). In general, the penetration

depth of the FSW pin should be approximately 0.2 mm above the bottom of the welded plate, as the shearing action from the tool pin is expected to be sufficient to fuse the weld at the bottom. This depth also protects the backing plate from deforming due to the high heat input. For the 6061 butt joint specimens, the penetration depth was set at 9.3 mm for the 9.5 mm thick aluminum plates. Similarly, for the 5083 plate, the penetration depth was set at 8.9 mm for the 9.1 mm thick aluminum plates. For the specimens with kissing bond and toe flash defects, the pin length was reduced to 8.4 or 8.5 mm. The plunge depth was then varied as needed to create each defect type. A penetration depth of 10.7 mm was used for the lap joint detail in order to ensure that the weld penetrated through the entire 9.5 mm plate thickness to create a horizontal initial crack-like defect (see Table 2).

Table 2: Welding process design for specimen fabrication.

Specimen type	Aluminum alloy	Plate thickness	Tool pin length (mm)	Tilt angle (°)	Rotation speed (rpm)	Travel speed (mm/min)	Plunge depth (mm)
Proper weld	6061	9.5	9.3	2.5	1120	63	9.3
Kissing bond			8.4				8.4
Toe flash			8.5				9.3
Lap joint			10.7				10.7
Proper weld	5083	9.1	8.9	2.5	1120	63	8.9
Wormhole						90	

60 fatigue tests were performed for this study in total. For each specimen type, at least four tests were completed under tension-only constant amplitude (CA) loading conditions at different stress ranges, ΔS (= $S_{max} - S_{min}$), a stress ratio, R (= S_{min} / S_{max}), of 0.1. For these tests, an effort was made to select stress ranges that would allow the slope of the finite life portion of the S-N curve, as well as an effective constant amplitude fatigue limit (CAFL), to be estimated. Tests that exceeded 3 million or so applied cycles without failure were identified as “runouts”. It should be noted that here that the term “runout” simply refers to a test that was stopped before failure (in this study, practical limitations prevented the

test from continuing further) – not a test for which an "infinite" fatigue life is necessarily expected. Following the CA loading tests, specimens were tested under a variable amplitude (VA) loading history for the support reaction on a 15 m long simply-supported beam subjected to measured highway traffic loading (see Figure 1(D)). This history was found in previous work to be a relatively severe one for aluminum welds in bridges [23].

The fatigue tests were performed in a 500 kN MTS structural testing frame at a frequency of 10-15 Hz. Specimen alignment was ensured using a "dummy" specimen, with gauges installed to measure the longitudinal strains on the four sides. This specimen was used on a regular basis to check the position of the stops, which controlled the specimen alignment. The formation of fatigue cracks was detected by visual inspection and the use of displacement limits, which stopped the test when there was a detectable change in the specimen stiffness. When a visible crack was detected, the crack surface was stained with dye penetrant, to enable measurement of the crack size and shape.

3. Fatigue Test Results

The stress-life (S-N) results of the fatigue test program are presented in Table 3 and Figures 3-6. In Table 3, the failure mode is also identified as a crack initiating from either the top of the weld on the advancing side (AR) – i.e. the side of the weld where the rotation and forward movement direction of the tool are the same, the top of the weld on the retreating side (RS), the bottom of the weld or weld root (WR), or the base metal (BM). The reported stress range, ΔS_{eq}, is simply $S_{max} - S_{min}$ for the CA tests. For the VA tests, a histogram of stress ranges in the 1000 peak repeating stress history was generated using a rainflow cycle counting algorithm. The Palmgren-Miner sum was then used to calculate ΔS_{eq}:

$$\Delta S_{eq} = \left(\sum_{i=1}^{k} \frac{\Delta S_i^{\,m} \cdot N_i}{N_{tot}} \right)^{1/m} \qquad (1)$$

where N_{tot} is the number of cycles in the history and ΔS_i and N_i are the stress ranges and number of cycles for each of the k stress range increments. In calculating the ΔS_{eq} values in Table 3, an S-N curve slope of m = 4.84 was assumed, which is the slope of the Cat. B design S-N curve for butt joints in [10]. This value was later varied to enable comparisons with different design curves.

Figure 3(A) presents the results for the "properly welded" 6061 specimens, along with the specimens fabricated with significant kissing bond defects, compared to the ADM Cat. B design curve. Looking at this figure, it can be seen that the results for the properly welded (PW) specimens all fall above the curve, whereas the specimens with kissing bond (KB) defects mostly fall below. It is concerning that there is considerable scatter in the PW data, and a number of PW points fall close to the design curve, contradicting the previous findings of others that this design curve is overly conservative. Further review revealed that the PW specimens exhibited a mixture of failure modes, and that the lower results in the data set can all be attributed to weld root (WR) failures. These results are circled in Figure 3.

A subsequent metallurgical analysis revealed that these specimens had KB defects with a depth of up to 344 μm at the weld root, even though they were fabricated with welding parameters established to avoid this. Thus, the results in Figure 3 could be considered as three data sets – PW specimens with top side (AS, RS, or BM) crack initiation sites, PW specimens with WR failures from small KB defects, and specimens with large, intentionally fabricated KB defects. In general, it can be seen that the CA and VA results line up reasonably well for each other for each of these three data sets.

In Figure 3(B), a similar comparison is made with the FAT 62 (m = 7) design curve proposed in [14]. Note that this design curve gets its name from the fact that it passes through a stress range of 62 MPa at N = 2 million cycles. Looking at this figure, it can be seen that all of the PW specimens with top side failures fall above the design curve. The PW specimens with WR failures straddle this design curve, and the KB specimens all fall below this design curve.

Table 3(a): Fatigue test results.

Test ID	Loading	S_{max} (MPa)	ΔS_{eq} (MPa)	N (10^3 cycles)	Failure	Defect[1]	Defect[2]
6061 Butt Joints, Properly Welded							
A6PW01B	CA	159.0	143.1	61079	BM		
A6PW01C	CA	120.0	108.0	828642	AS		
A6PW01D	CA	112.5	101.2	741302	BM		
A6PW02A	CA	90.0	81.0	3255068	Runout		
A6PW02B	CA	105.0	94.5	6017249	Runout		
A6PW02C	CA	135.0	121.5	420979	AS		
A6PW02D	CA	150.0	135.0	276560	RS		
A6PW03A	CA	165.0	148.5	33235	WR	332 µm (JLR)	
A6PW03C	CA	177.0	159.3	48356	AS and WR	344 µm (JLR)	
A6PW04A	VA	166.3	65.0	492437	WR		
A6PW04B	VA	102.3	40.0	4112113	WR		
A6PW04C	VA	144.4	56.5	858770	WR		
A6PW05A	VA	127.9	50.0	7724571	AS		
A6PW05C	VA	166.3	65.0	5383609	RS		
6061 Butt Joints, Kissing Bond Defect							
A6KB01A	CA	120.0	108.0	13506	WR	1.10±0.06 mm	1.05± 0.03 mm
A6KB01B	CA	90.0	81.0	57581	WR	1.11±0.08 mm	1.00±0.03 mm
A6KB01C	CA	60.0	54.0	5322591	Runout	1.20±0.03 mm	
A6KB01D	CA	75.0	67.5	135466	WR		0.97±0.04 mm
A6KB02A	VA	127.9	50.0	342040	WR	1.00±0.02 mm	0.90±0.03 mm
A6KB02B	VA	76.8	30.0	10176309	Runout	1.03±0.01 mm	
A6KB02C	VA	102.3	40.0	1692092	WR	1.01±0.03 mm	0.87±0.02 mm
A6KB02D	VA	89.5	35.0	4613013	WR		0.85±0.06 mm
A6KB03A	VA	153.5	60.0	213159	WR	1.02±0.04 mm	0.93±0.02 mm
A6KB03B	VA	127.9	50.0	458736	WR	1.02±0.04 mm	0.89±0.03 mm
A6KB03C	VA	102.3	40.0	2017588	WR	1.00±0.03 mm	0.85±0.02 mm
A6KB03D	VA	89.5	35.0	1791686	WR		0.8±0.03 mm
6061 Lap Joints							
A6LJ01A	CA	120.0	108.0	13693	WR	453 µm	
A6LJ01B	CA	90.0	81.0	64970	WR	599 µm	
A6LJ01C	CA	75.0	67.5	126227	WR	449 µm	
A6LJ01D	CA	60.0	54.0	219378	WR		
A6LJ02A	CA	45.0	40.5	563711	WR	455 µm	
A6LJ02B	CA	30.0	27.0	5338486	WR	292 µm	
A6LJ02C	VA	76.8	30.0	2144792	WR	313 µm	
A6LJ02D	VA	51.2	20.0	9419241	WR		
A6LJ03A	VA	89.5	35.0	923005	WR	262 µm	
A6LJ03B	VA	89.5	35.0	1395342	WR	384 µm	
A6LJ03D	VA	115.1	45.0	494469	WR	376 µm	

Table 3(b): Fatigue test results (cont'd).

Test ID	Loading	S_{max} (MPa)	ΔS_{eq} (MPa)	N (10^3 cycles)	Failure	Defect[1]	Defect[2]
6061 Butt Joints, Toe Flash Defect							
A6TF01A	CA	150.0	135.0	55846	AS		
A6TF01B	CA	120.0	108.0	114016	AS		
A6TF01C	CA	90.0	81.0	520841	AS		
A6TF01D	CA	105.0	94.5	418103	AS		
A6TF02B	CA	75.0	67.5	467218	WR	700 µm	0.62±0.04 mm
A6TF02C	VA	166.3	65.0	290734	WR	629 µm	0.63±0.03 mm
A6TF02D	VA	153.5	60.0	349585	WR		
A6TF03A	VA	181.5	71.0	1009218	WR	356 µm (JLR)	
A6TF03B	VA	146.2	57.2	5497205	Runout	324 µm (JLR)	
A6TF03C	VA	102.3	40.0	10001506	Runout		
A6TF03D	VA	115.1	45.0	11082046	Runout		
5083 Butt Joints, Properly Welded							
A5PW02A	CA	125.6	113.0	92467	AS and WR		
A5PW02B	CA	109.9	98.9	5606722	Runout		
A5PW02C	CA	141.3	127.2	2992566	Runout		
A5PW02D	CA	172.7	155.4	94494	WR		
A5PW03A	CA	157.0	141.3	404680	WR	33 µm (JLR)	
A5PW03B	CA	164.8	148.4	238098	WR	160 µm (JLR)	
A5PW03C	CA	149.1	134.2	390320	WR	365 µm (JLR)	
A5PW03D	CA	149.1	134.2	99589	WR		
5083 Butt Joints, Wormhole Defect							
A5WH01A	CA	125.6	113.0	139337	WH		0-2.46 mm
A5WH01B	CA	109.9	98.9	408156	WR		
A5WH01C	CA	94.2	84.8	338064	WH		0-2.76 mm
A5WH01D	CA	78.5	70.6	2951	WH		3.18±0.16 mm

Notes: ΔS_{eq} shown in this table for VA tests is value calculated using Palmgren-Miner sum with m = 4.84.
N = number of cycles required to fracture specimen into two pieces.
BM = base metal, AS = advancing side, RS = retreating side, WR = weld root
1 = cross section measurement, 2 = fracture surface measurement, JLR = joint line remnant

Figure 4 presents similar results for the 6061 lap joint (LJ) specimens. Looking at Figure 4(A) it can be seen that the results for the specimens in this series generally fall below the ADM Cat. B design curve. For this test series, the results can also be seen to exhibit minimal scatter, with the CA and VA results lining up well with each other. In Figure 4(B), the results are compared with the ADM Cat. D design curve (m = 3.73). Qualitatively, it seems that this curve would be a more satisfactory one for use with

this detail, as all of the data points except one fall above it. To confirm this, a statistical procedure recommended by the International Institute of Welding (IIW)[24] was used to establish mean and design S-N curves for this detail, for which relatively little test data currently exists. Looking at Figure 4(B), it can be seen that the calculated design (95% survival probability) curve is slightly above the ADM Cat. D design curve.

Figure 3: Fatigue test results for 6061 PW and KB specimens compared with: (A) ADM Cat. B design curve, and (B) FAT 62 (m = 7) design curve from [14].

Figure 4: Fatigue test results for 6061 LJ specimens compared with: (A) ADM Cat. B design curve, and (B) ADM Cat. D design curve.

Figure 5 presents results for the TF specimens with toe flash defects intentionally introduced by excessive tool penetration. The data for this defect type shows more scatter than that of the KB and LJ data sets. The explanation for this is that – similar to the PW data set – the TF specimens exhibited two failure modes. Specifically, failures were observed at the AS and WR locations. The WR failures are circled in Figure 5 and generally fell on or below the AS failure data. Comparing the results to the ADM Cat. B design curve in Figure 5(A), it can be seen that all of the results fall above this curve except for two points corresponding with WR failures. In Figure 5(B), the results are compared with the FAT 62 (m = 7) design curve proposed in [14]. Again, all of the results fall above this design curve except for three points corresponding with WR failures.

Figure 5: Fatigue test results for 6061 TF specimens compared with: (A) ADM Cat. B design curve, and (B) FAT 62 (m = 7) design curve from [14].

Figure 6 shows the results for the 5083 PW specimens and specimens fabricated with wormhole (WH) defects introduced. Only CA tests were performed for these two specimen types. For comparison

purposes, the 6061 PW CA results are plotted, along with the ADM Cat. B design curve, and the FAT 62 (m = 7) design curve from [14]. Looking at this figure, it can be seen that the 5083 PW results all fall above both design curves. If an effective CAFL were to be established using the runout data, it appears that it would be slightly higher for the 5083 alloy. The results for the WH specimens show a very high level of scatter, and no clear linearly decreasing trend as was seen for the other data sets. The reason for this result, as well be discussed in the next section, was the high level of difficulty encountered in creating this defect type with any consistency in the size or degree of continuity.

Figure 6: Fatigue test results for 5083 PW and WH specimens compared with ADM Cat. B design curve FAT 62 (m = 7) design curve from [14].

4. Metallurgical Analysis Results

A broad range of destructive and non-destructive evaluation (NDE) techniques were employed with the goal of quantifying the FSW joint properties and defect severity at various stages during this experimental study. The KB defects in the various specimen types, including the specimens with significant KB defects intentionally fabricated were not visible on the bottom surface to the naked eye. In order to investigate how these defects might be detected in practice, several NDE techniques were performed on the WR location of the specimens in the KB series, including radiographic (RT), liquid penetrant (LP), and ultrasonic (UT) inspection, by an external laboratory. Initial attempts to detect the KB defects were unsuccessful regardless of the method used. Subsequent efforts using UT with the phased array method were more successful. The best results were obtained using this method with the 45° linear technique. Further details on these NDE efforts can be found in [25].

Metallographic analysis was performed on the scrap material between the dog-bone specimens. Samples were cut from this material, mounted in epoxy, and ground, polished, and etched using Keller's reagent

so that the cross section of the weld nugget could be viewed under a microscope and so that hardness measurements at various locations on the weld profile could be obtained.

Vickers microhardness was obtained using a 200 g force load with a 10 s dwell time. Results of these measurements are presented in Figure 7. The hardness values in Figure 7(a) were measured horizontally at the mid-thickness, while Figures 7(b) and (c) are representative cross sectional hardness maps of the stir zones of 6061 and 5083 samples, respectively. Looking at Figure 7(a), it can be noted that the differences between the A6PW, A6TF, and A6LJ samples are minimal. The hardness values measured in the heat affected zones (HAZs) were the lowest on each side of the weld nugget zone (NZ) for the heat-treatable 6061 alloy, forming a "W" shaped hardness profile for the A6PW, A6TF, and A6LJ samples. This softening of the HAZ is expected in heat treatable alloy welds and is due to the coarsening of the strengthening precipitates caused by heat from the welding process [26-28].

The hardness profiles in Figure 7 also suggests that the fatigue strength for the non-heat-treatable 5083 alloy was less influenced by heat during the FSW process, therefore resulting in a higher hardness profile than the 6061 alloy. The measured hardness values across the weld profile for the 5083 alloys were relatively uniform, with negligible hardness changes across the welding profile. This may explain in part why the majority of failures in the 5083 samples initiated from the WR and WH locations, since there is no significant softened region prone to localized straining for this alloy.

Figure 7: Microhardness measurements: (A) mid-thickness, (B) 6061, and (C) 5083.

Kissing bond (i.e. WR) defect depths were measured on both the polished cross section samples and the fracture surfaces of specimens that were observed to have failed by crack initiation at the WR location. Figure 8 shows sample images of WR defects observed in the cross section samples. For the KB specimens, the WR defect was on the order of 1 mm in depth and was initially straight and perpendicular to the bottom edge of the specimen. Further within the thickness of the plate the kissing

bond deflects towards the AS direction and becomes parallel to the plate surface. The minor WR defects observed in the PW specimens tended to appear as a straight fold aligned at a shallow angle with respect to the specimen bottom edge. The crack-like defects observed in the LJ specimens, which also resulted in WR failures, were hook-shaped. They started out in a horizontal direction, parallel to the specimen bottom edge, and then turned upwards near the NZ edge, possibly due to upward flow of the plasticized material in this region.

Identifying the precise location of the defect tips was made difficult by the fact that in many cases the tips were not distinct, but rather the defect gradually transitioned into a discontinuous joint line remnant (JLR). In Table 3, the results of the KB defect depth measurements are tabulated. The cross section samples obtained from the scrap material adjacent to a given fatigue specimen were deemed to provide a representative indication of the defect depth within the specimen. The cross section measurements were verified by measurements made on the fracture surfaces (see Figure 9) using an optical microscope. Although the fracture surface measurements were potentially affected by plastic deformation that may have preceded the specimen fracture, these measurements were useful for verifying the continuity of the defect across the specimen width. These measurements are reported as depths perpendicular to the loading direction, recognizing that the actual defect shape is more complex. For the planned fracture mechanics analysis, however, this dimension was thought to be the simplest and most practical way of characterizing the defect size. Where the defects transitioned to a JLR, judgement was used to determine the depth at which the defect ceased to be continuous. Table 3 indicates cases where the defect appeared to consist entirely of JLR. This was typically the case for the small defects observed in the PW specimens.

Figure 8: WR defect measurements in (A) KB, (B) PW, and (C) LJ specimens.

Figure 9: Fracture surface of specimen with kissing bond defect.

Figure 10 shows an example of the cross-sectional weld profile for one of the specimens with toe flash due to excessive tool penetration. While the toe flash generated in the fabrication of these specimens was readily apparent, it is the loss of cross section and the sharp stress concentration resulting from the excess tool penetration that are thought to be more detrimental from a fatigue perspective. In general, the thickness reduction for these specimens was on the order of 0.5 mm at the nugget centre. This reduction reduced by half at the edges of the tool / nugget zone. The radius of the transition was similar to the tool shoulder radius of 0.15 mm.

Figure 10: Weld profile of specimen with toe flash defect.

Figure 11 shows typical fracture profiles for TF, KB, and LJ specimens. In this figure, the extents of the weld NZ are denoted with dashed lines and the fracture direction is also indicated. The typical failure mode for the TF specimens was a crack initiating on the AS, and propagating through the HAZ. For the KB specimens, the cracks initiated from the WR and propagated through the NZ. For the LJ specimens, the cracks initiated from tip of the WR defect and propagated through the NZ.

Figure 11: Fracture profiles for (A) TF, (B) KB, and (C) LJ specimens.

Figure 12 presents fracture surface photos for the three A5WH specimens with detectable WH defects. In this figure, the defect irregularity can be seen. While the original goal was to produce subsurface defects, the produced defects broke the surface, which means they are more severe from a fatigue perspective and likely would be detected by visual inspection. In Table 3, WH depths are estimated for each specimen, based on microscope images of the fracture surfaces. While the results of this study show the effect that WH defects can have on fatigue performance, further study would be needed to establish a relationship between WH severity and fatigue performance.

Figure 12: Wormhole defects in specimens (A) A5WH01A, (B) A5WH01C, and (C) A5WH01D.

5. Fracture Mechanics Analysis

Following the fatigue testing and metallurgical analysis, a fracture mechanics analysis was conducted to facilitate further understanding of the effects of several of the investigated defect types and demonstrate that the experimental results could be predicted with a reasonable accuracy using this approach. The analyzed defects included those observed in the 6061 PW, KB, TF, and LJ specimens.

Further details of the strain-based fracture mechanics (SBFM) model used in this analysis can be found in [23, 29-31]. The basis for this model is the Paris-Erdogan crack growth law, commonly used in linear elastic fracture mechanics (LEFM), modified to consider crack closure effects and a threshold stress intensity factor (SIF) range, ΔK_{th}, and integrated over a crack depth range, a_i to a_c:

$$N = \int_{a_i}^{a_c} \frac{\mathrm{d}a}{C \cdot \mathrm{MAX}\left(\Delta K_{eff}{}^{m} - \Delta K_{th}{}^{m}, 0\right)} \qquad (2)$$

where C and m are material constants. The effective SIF range, ΔK_{eff}, considering crack closure (or opening) stress effects, is determined by the following expression:

$$\Delta K_{eff} = K_{max} - \mathrm{MAX}\left(K_{op}, K_{min}\right) \qquad (3)$$

where K_{max} and K_{min} are the SIFs due to the maximum and minimum local strain levels (ε) for each load cycle and K_{op} is the SIF corresponding with the crack opening strain level for a given load cycle. The following expression is used to calculate each of the required SIFs:

$$K = Y \cdot E \cdot \varepsilon \cdot \sqrt{\pi \cdot (a + a_0)} \qquad (4)$$

where a_0 is a material constant to account for small crack behaviour and Y is a correction factor to account for the crack shape, the free surface on one side of the crack, and the finite thickness of the cracked plate. The constant a_0 can be calculated as follows:

$$a_0 = \left(\frac{\Delta K_{th}}{\Delta \sigma_e} \right)^2 \cdot \frac{1}{\pi} \qquad (5)$$

where $\Delta\sigma_e$ is the fatigue limit for R = -1 ($\approx 0.5 \cdot \sigma_u$).

To calculate the stresses and strains, σ and ε, for each load cycle, a Ramberg-Osgood material model is used, which requires the cyclic material parameters: K' and n'. Strain histories are determined using Neuber's rule. Crack closure is modelled using formulas by Newman [32]. These require the maximum stress, σ_{max}, the stress ratio, R, the flow stress, σ_0, and a plastic constraint factor, α.

As discussed in [29,30], the primary advantage of the SBFM model is its ability to model nonlinear material effects such as crack closure and the effects of changes in the residual stress level following overload or underload events in VA loading histories. Another significant advantage of this model, is that it does not require two stages to model the total fatigue life of the weld. Since it was developed to model small crack behaviour in notches, where material behaviour is nonlinear, it does not run into the problems of LEFM in this domain. For larger crack sizes, the results converge on those calculated by LEFM. Table 4 provides values for the input parameters used in this analysis.

Table 4: Input parameters used in fracture mechanics analysis.

Parameter	Value	Units
t	9.5	mm
E	64011	MPa
σ_y	134.1	MPa
σ_u	181.5	MPa
LN(C)	-30.6	MPa, mm
m	4.0	MPa, mm
ΔK_{th}	45.0	MPa·√mm
K'	304.5	MPa
n'	0.13	-
μ	0.003	-

Regarding these input parameters, the following comments can be made:

- E, σ_y, σ_u, K', and n' were estimated based on the hardness measurements reported herein and interpolating between the measured properties for 6061 alloy T651 and O tempers from [23].
- LN(C), m, ΔK_{th}, and μ values were similar to the values used in [14,23], which are intended to represent averages of measured data for 5xxx and 6xxx series alloys.

In addition to these input parameters, implementation of the fracture mechanics model requires the local elastic stress distribution along the anticipated crack path and the initial defect size and shape. The elastic stress distribution was assumed to be uniform for the PW and KB specimens. For the TF and LJ specimens, the stress distributions were obtained by finite element analysis using the software ABAQUS. 2D plane strain models were used to obtain stress concentration factors (SCFs) relating the nominal stress in the plate to the local elastic stress along the crack path. The resulting SCF distributions along the crack paths for these specimen types are shown in Figure 13. The initial crack depths assumed in the analysis were: 1.0 mm for the KB specimens, 0.3 mm for the PW specimens with WR failures due to unexpected KB defects, and 0.6 mm for the LJ specimens, which were considered to be characteristic defect sizes, based on the measurements reported in Table 3. All of these defects were considered as through-cracks (running the full 70 mm specimen width), based on the observed defect shapes and fracture surfaces. For the topside failures in the PW and TF specimens, a 0.15 mm initial defect depth was assumed, which is the radius of the FSW tool shoulder. Based on crack shape measurements reported in [25], a crack aspect ratio (depth / half width) of 0.55 was assumed. This was the average of the measured crack aspect ratios for larger cracks, based on measurements made on fracture surfaces stained with dye penetrant prior to total specimen fracture. In the analysis, a uniform, tensile residual stress of 8.45 MPa was assumed, as recommended in prior work [14]. Analyses were performed under CA loading and under the VA loading history used in the experimental study (see Figure 1(D)).

Figure 13: SCF distributions for: (A) lap joint, and (B) toe flash specimens.

Figures 14 and 15 present the results of the performed SBFM analyses. In these figures, the solid lines represent CA analysis results and the dashed lines represent VA results. Looking at these figures, it can be seen that the SBFM model does a reasonable job of predicting a number of the key trends observed in the experimental results. In Figure 14, comparisons are presented for the 6061 PW and KB specimens. In general, the analysis results with a 1.0 mm WR defect assumed provide accurate or slightly conservative predictions for the KB specimens. For the PW specimens, the WR failures follow the SBFM curves with a 0.3 mm WR defect assumed. The topside failures are predicted reasonably well by the analysis with a 0.15 mm semi elliptical defect with a crack aspect ratio of 0.55. The predictions are somewhat on the high side though at the higher stress ranges. Similar trends and a similar level of prediction accuracy can be seen in Figure 15 for the LJ and TF specimens.

Figure 14: SBFM results for 6061 PW and KB specimens.

Figure 15: SBFM results for 6061 LJ (A) and TF (B) specimens.

6. Conclusions

Based on the fatigue test results, metallurgical analysis, and nonlinear fracture mechanics analysis presented in this paper, the following main conclusions are drawn:

- The properly welded FSW butt joints were generally seen to achieve fatigue lives above the ADM Cat. B. and FAT62 (m = 7.0) design curves.
- Kissing bond (KB) defects on the order of 0.3-1.0 mm in depth in 6061-T651 alloy specimens generally resulted in a significant fatigue life reduction and a shift in the failure mode from crack initiation on the weld topside to crack initiation at the weld root.
- The investigated toe-flash (TF) defect had a less significant effect on fatigue performance.

- The tested lap joint (LJ) detail resulted in a lower fatigue life than that of the butt joint detail, which could be safely estimated using the ADM Cat. D design curve.
- It was found that the fatigue test results could be predicted reasonably well, using a nonlinear fracture mechanics (SBFM) model with typically assumed input parameters for 5xxx and 6xxx series alloys and knowledge of the initial defect geometry.

7. Acknowledgments

Funding for this research provided by the Aluminum Association of Canada (AAC) and the National Science and Engineering Research Council of Canada (NSERC) is gratefully acknowledged. Assistance with the fatigue testing provided by R. Morrison, P. Volcic, and S. Arbuckle is also acknowledged.

8. References

[1] Lohwasser, D. & Chen, Z. (2010). Friction stir welding: From basics to applications. Woodhead Publishing Limited, Cambridge, England.

[2] Svensson, L.-E., Karlsson, L., Larsson, H., Fazzini, M., & Karlsson, J. (2000). Microstructure and Mechanical Properties of Friction Stir Welded Aluminum Alloys with Special Reference to AA5083 and AA6082. Science and Technology of Welding and Joining, pp. 285-296.

[3] Mishra, R. & Mahoney, M. (2007). Friction Stir Welding and Process. Ohio: ASM International.

[4] Walbridge, S. & de la Chevrotiere, A. (2012). Opportunities for the use of Aluminum in Vehicular Bridge Construction. Aluminum Association of Canada Report.

[5] Kou, S. (2003). Welding Metallurgy. John Wiley & Sons Inc., New Jersey, USA.

[6] International Standards Organization. (2011). “ISO 25239: Friction stir welding – Aluminium”.

[7] American Welding Society. (2014). “AWS D1.2: Structural Welding Code – Aluminum”.

[8] Canadian Standards Association. (2013). "CAN/CSA W59.2: Welded Aluminum Construction".

[9] European Committee for Standardization. (2007). "Eurocode 9: Design of Aluminum Structures".

[10] The Aluminum Association. (2015). "Aluminum Design Manual Part I: Specification for Aluminum Structures".

[11] Canadian Standards Association. (2014). "CAN/CSA S157: Strength Design in Aluminum".

[12] Dickerson, T. & Przydatek, J. (2003). Fatigue of Friction Stir Welds in Aluminum Alloys that Contain Root Flaws. International Journal of Fatigue, pp. 1399-1409.

[13] Svensson, L.-E., Karlsson, L., Larsson, H., Fazzini, M., & Karlsson, J. (2000). Microstructure and Mechanical Properties of Friction Stir Welded Aluminum Alloys with Special Reference to AA5083 and AA6082. Science and Technology of Welding and Joining, pp. 285-296.

[14] Miranda, A.C. de O., Gerlich, A., & Walbridge, S. (2015). Aluminum friction stir welds: Review of fatigue parameter data and probabilistic fracture mechanics analysis. Engineering Fracture Mechanics, 147, pp. 243–260.

[15] Lin, P. C., Lo, S. M., & Wu, S. P. (2018). Fatigue life estimations of alclad AA2024-T3 friction stir clinch joints. International Journal of Fatigue, 107, pp. 13-26.

[16] Sun, G., Chen, Y., Wei, X., Shang, D., & Chen, S. (2018). Crystal plastic modeling on fatigue properties for aluminum alloy friction stir welded joint. Materials Science and Engineering: A, 728, pp. 165-174.

[17] Sun, G., Chen, Y., Chen, S., & Shang, D. (2017). Fatigue modeling and life prediction for friction stir welded joint based on microstructure and mechanical characterization. International Journal of Fatigue, 98, pp. 131-141.

[18] Wang, W., Qiao, K., Wu, J. L., Li, T. Q., Cai, J., & Wang, K. S. (2017). Fatigue properties of friction stir welded joint of ultrafine-grained 2024 aluminium alloy. Science and Technology of Welding and Joining, 22(2), pp. 110-119.

[19] Rodriguez, R. I., Jordon, J. B., Allison, P. G., Rushing, T., & Garcia, L. (2016). Low-cycle fatigue of dissimilar friction stir welded aluminum alloys. Materials Science and Engineering: A, 654, pp. 236-248.

[20] American Society for Testing and Materials. (2017). "ASTM E1097 - 12: Standard Guide for Determination of Various Elements by Direct Current Plasma Atomic Emission Spectrometry".

[21] American Society for Testing and Materials. (2011). "ASTM E1479 – 99: Standard Practice for Describing and Specifying Inductively-Coupled Plasma Atomic Emission Spectrometers".

[22] Kadlec, M., Růžek, R., & Nováková, L. (2015). Mechanical behaviour of AA 7475 friction stir welds with the kissing bond defect, International Journal of Fatigue, 74, pp. 7-19.

[23] Coughlin, R., & Walbridge, S. (2012). Fatigue Testing and Analysis of Aluminum Welds under In-Service Highway Bridge Loading Conditions. Bridge Engineering, 17(3).

[24] Hobbacher, A. (2005). Recommendations for fatigue design of welded joints and components, International Institute of Welding Doc. XIII-1965-03/XV-1127-03.

[25] Guo. S. (2018). Fatigue Behaviour of Aluminum Friction Stir Welds Under Highway Bridge Loading Conditions, University of Waterloo MASc Thesis.

[26] Mathers, G. (2002). The welding of aluminium and its alloys. Woodhead Publishing Limited, Cambridge, England.

[27] Song, Y. (2014). Defect features and mechanical properties of friction stir lap welded dissimilar AA2024–AA7075 aluminum alloy sheets. Materials & Design, 55, pp. 9-18.

[28] Woo, W. & Choo H. (2011). Softening behaviour of friction stir welded Al 6061-T6 and Mg AZ31B alloys. Sci. Technol. Weld. Join. 16(3), pp. 267–272.

[29] Ranjan, R., Ghahremani, K., Walbridge, S., & Ince, A. (2016). Testing and fracture mechanics analysis of strength effects on the fatigue behavior of HFMI-treated welds. Welding in the World.

[30] Ghahremani, K. & Walbridge, S. (2011). Fatigue testing and analysis of peened highway bridge welds under in-service variable amplitude loading conditions, International Journal of Fatigue, 33, pp. 300-312.

[31] M. Khalil, M. & Topper, T.H. (2003). Prediction of crack-opening stress levels for 1045 as-received steel under service loading spectra, International Journal of Fatigue, 25(2), pp. 149-157.

[32] Newman, J.C. (1994). A Crack Opening Stress Equation for Fatigue Crack Growth, International Journal of Fracture, 24, pp. R131-R135.

Highlights

- 0.3-1.0 mm kissing bond defects led to a fatigue life reduction in FSW joints
- Investigated toe flash / undercut defect had less of an effect on fatigue life
- Tested FSW lap joint detail had lower fatigue life than the butt joint detail
- Fatigue test results predicted with nonlinear fracture mechanics (SBFM) model

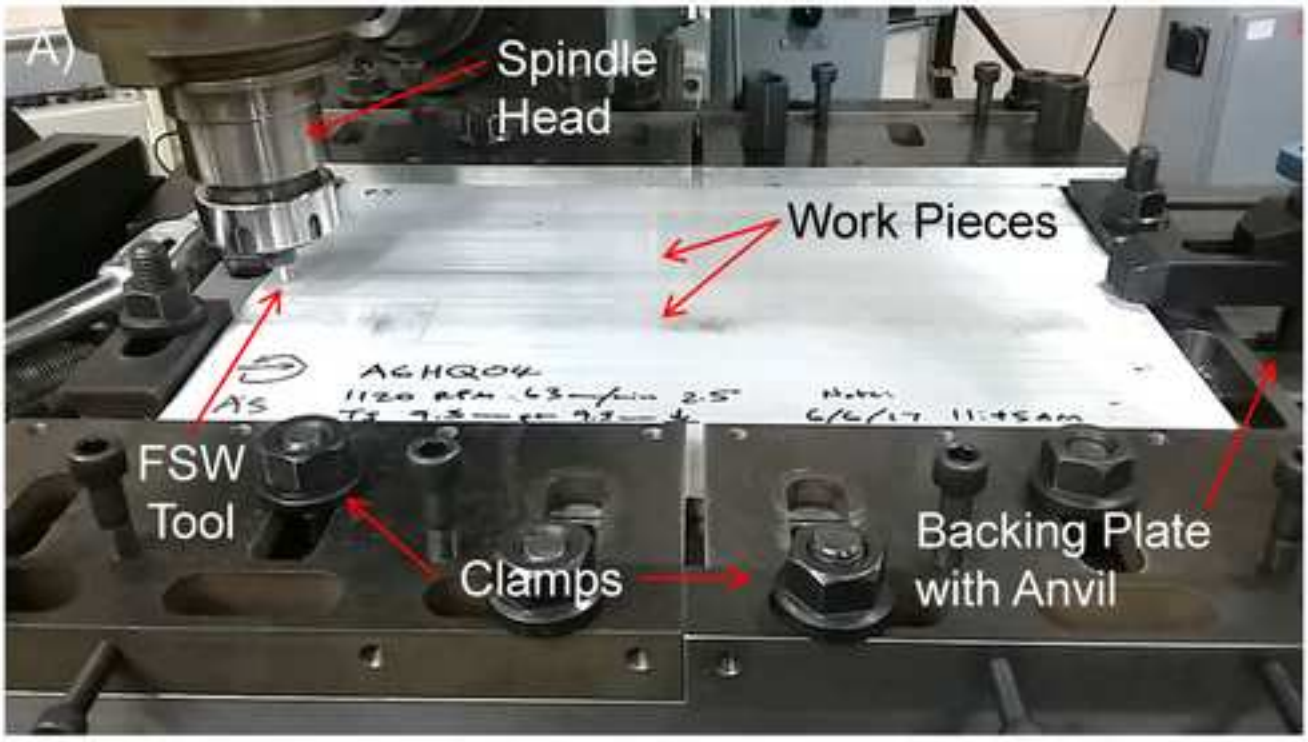

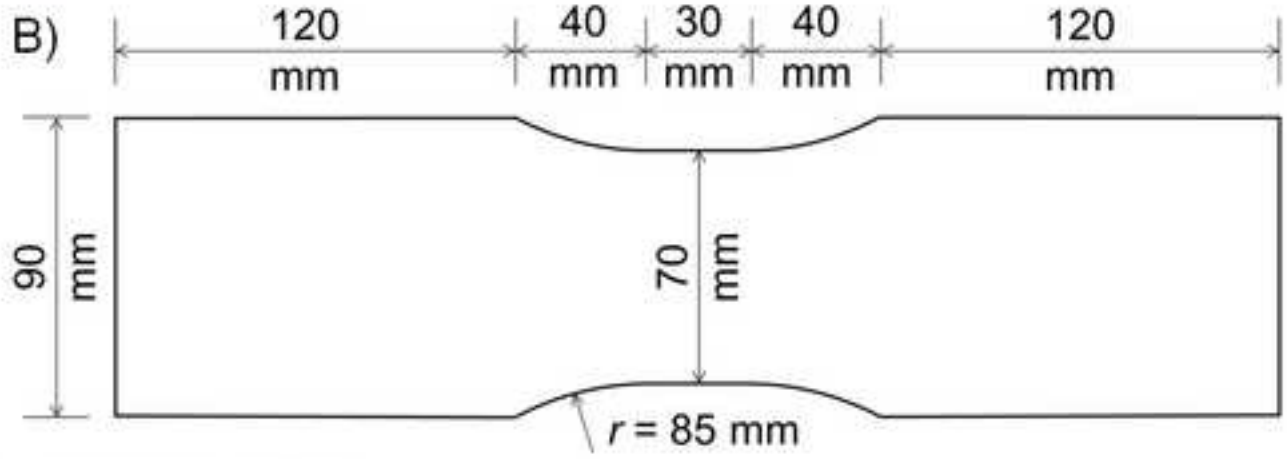

10° tapered, M6 threaded three flats H13 steel tool

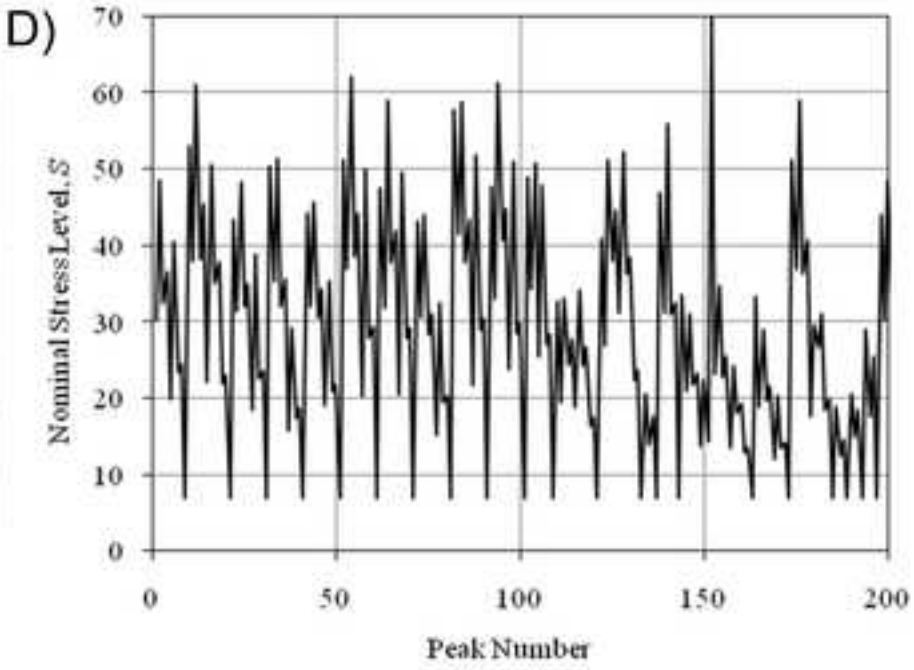

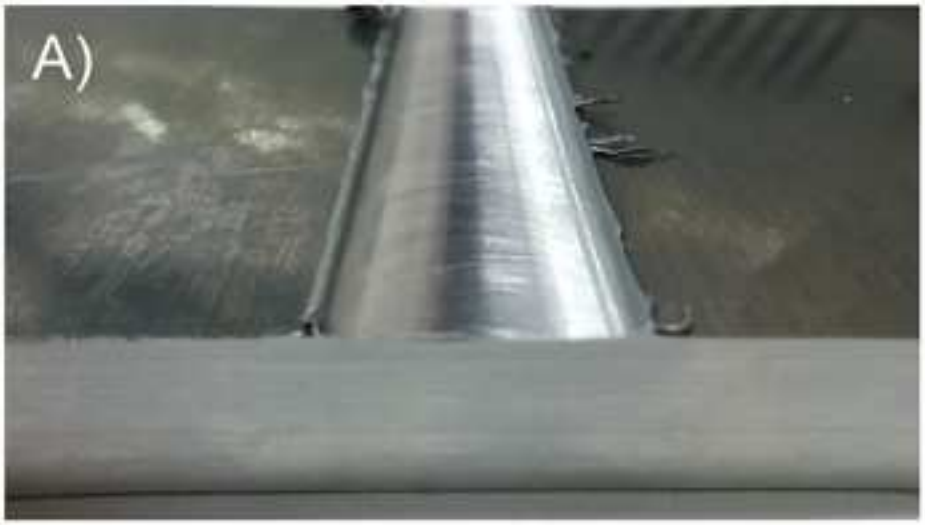

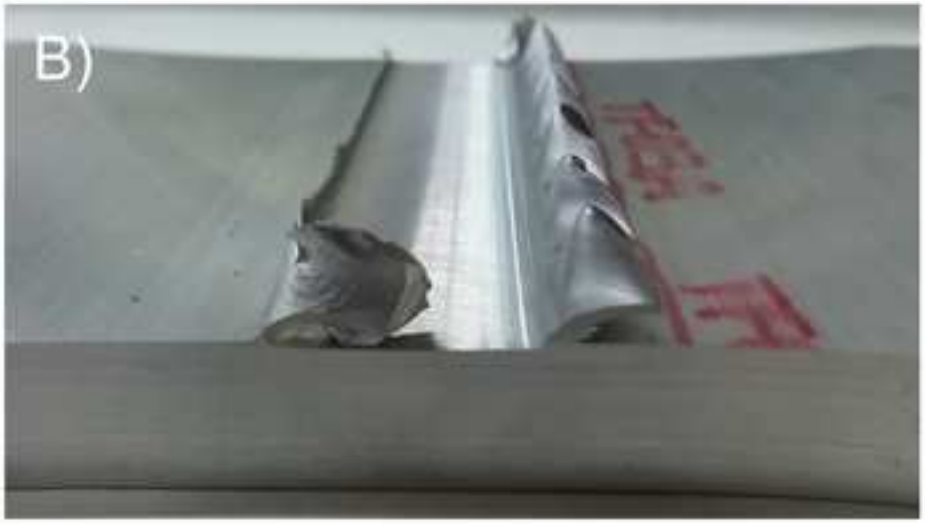

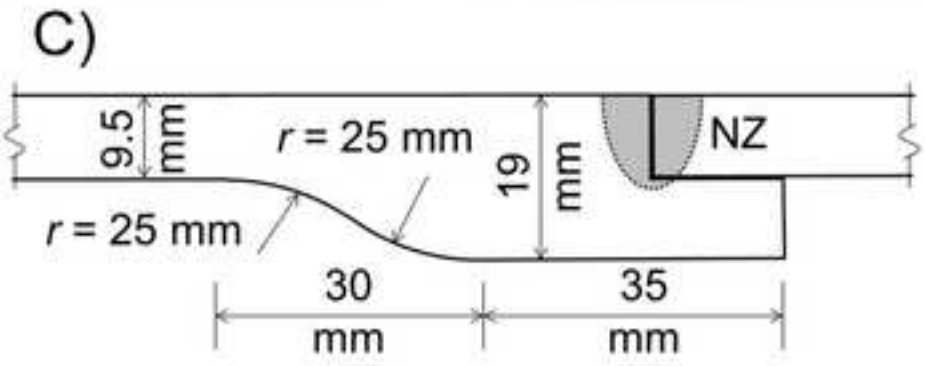

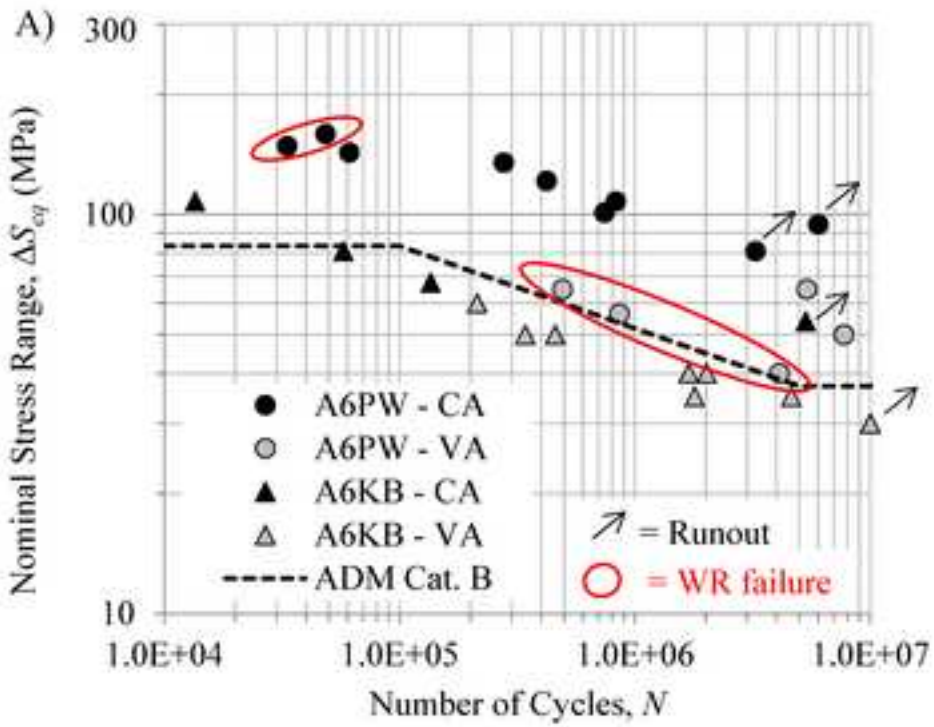

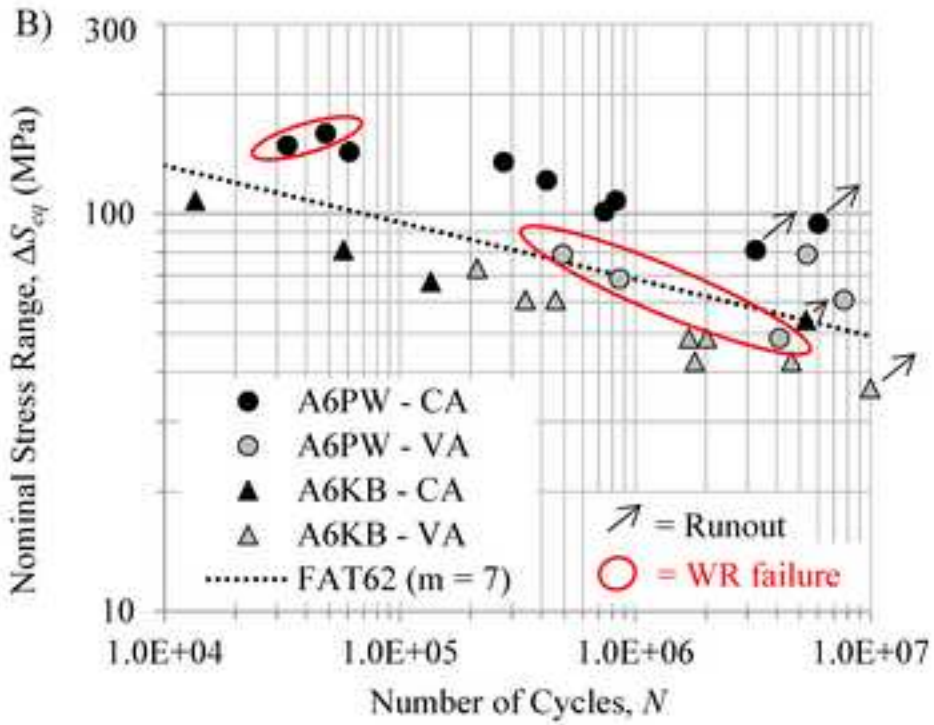

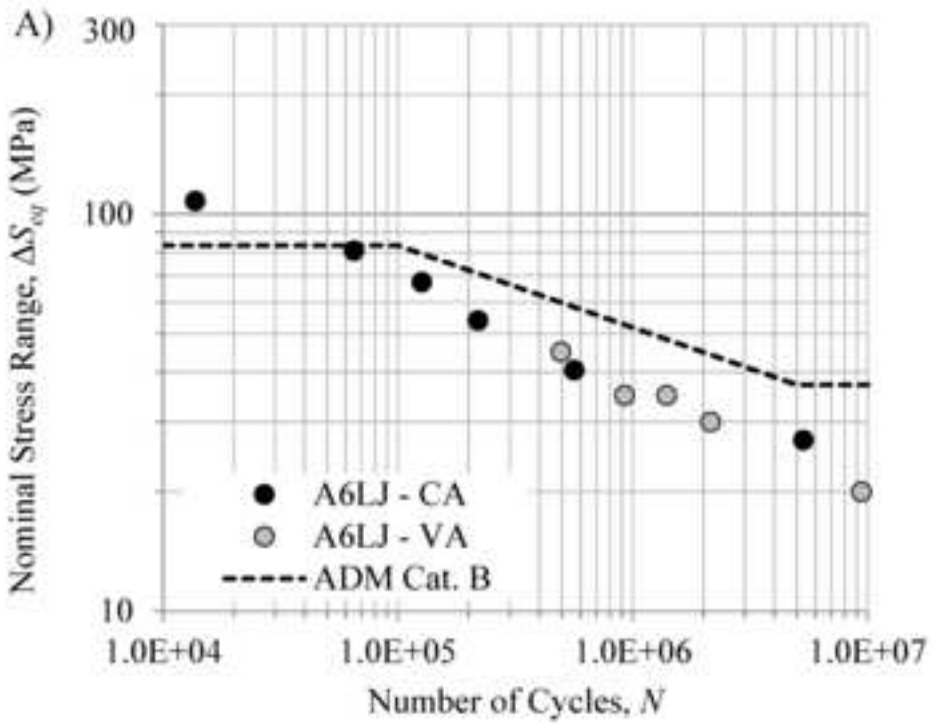

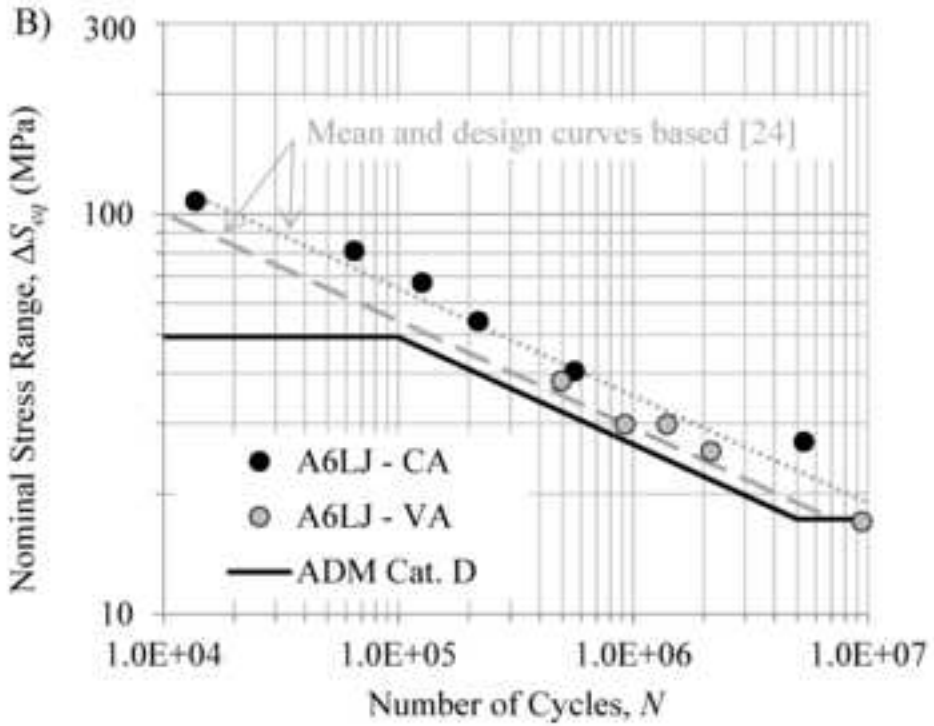

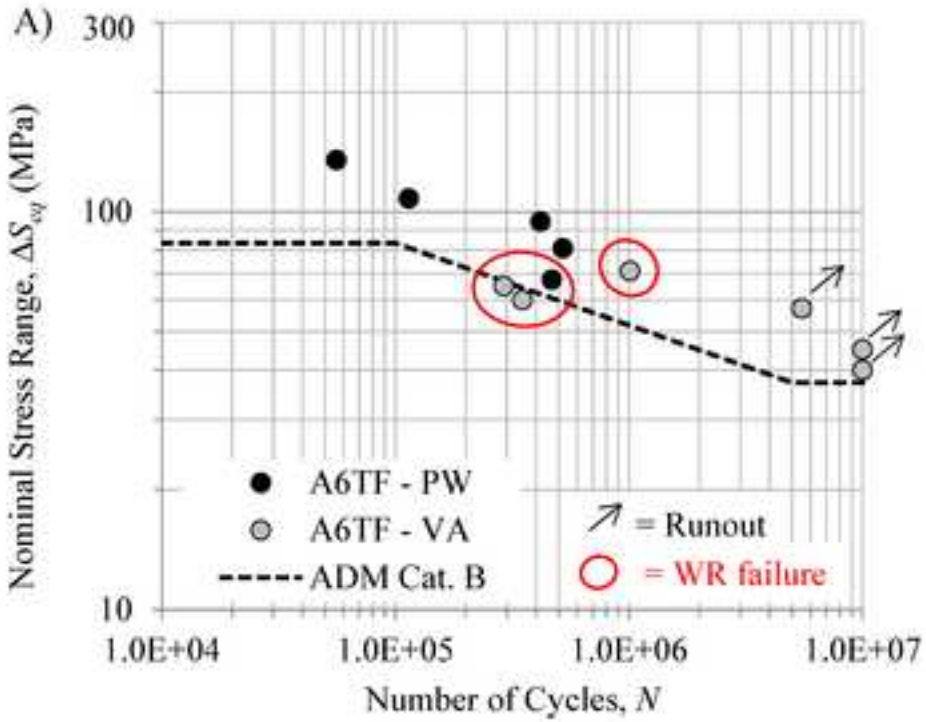

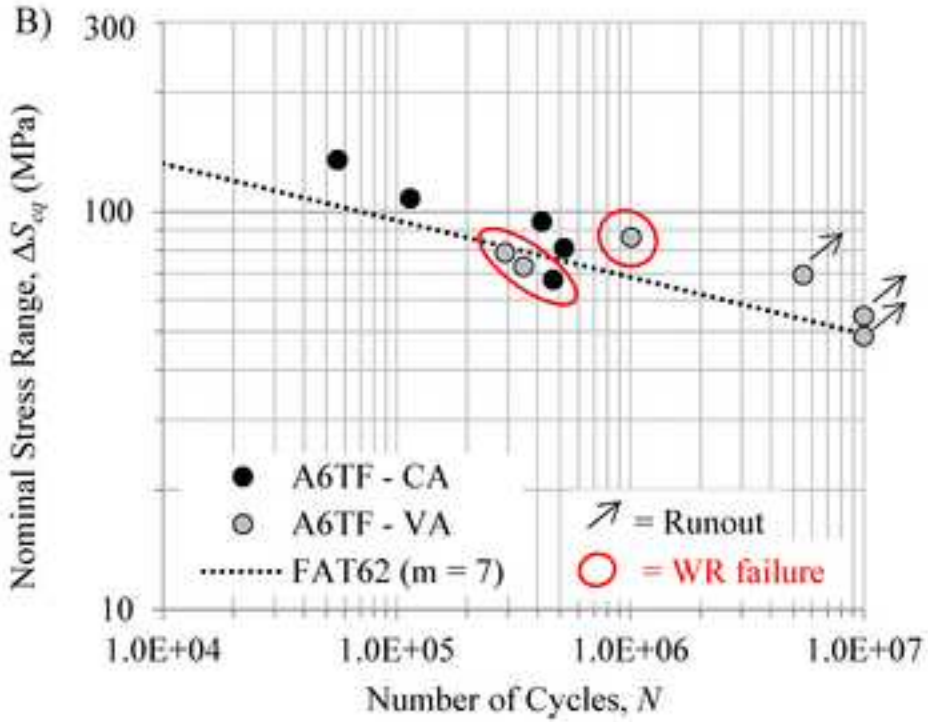

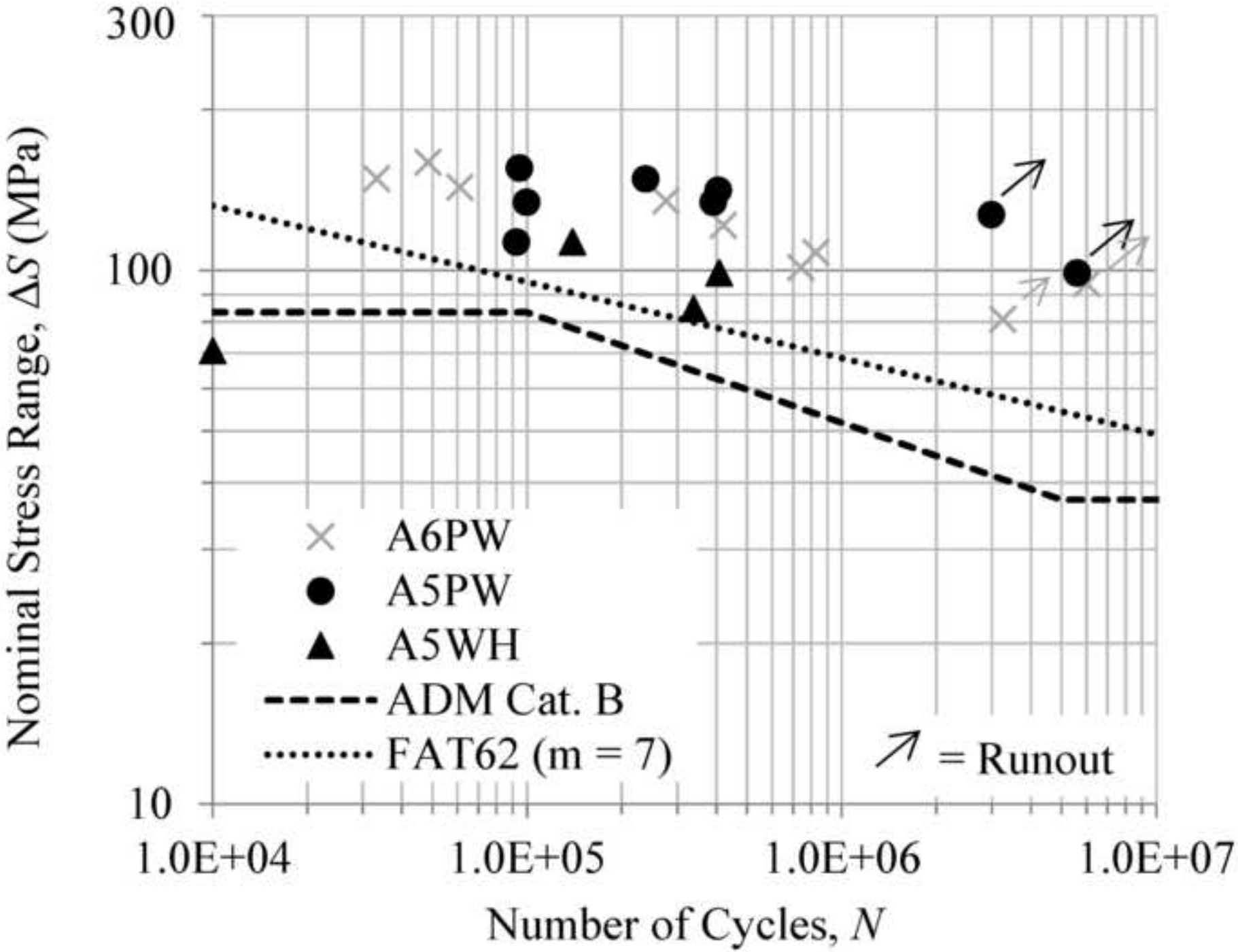

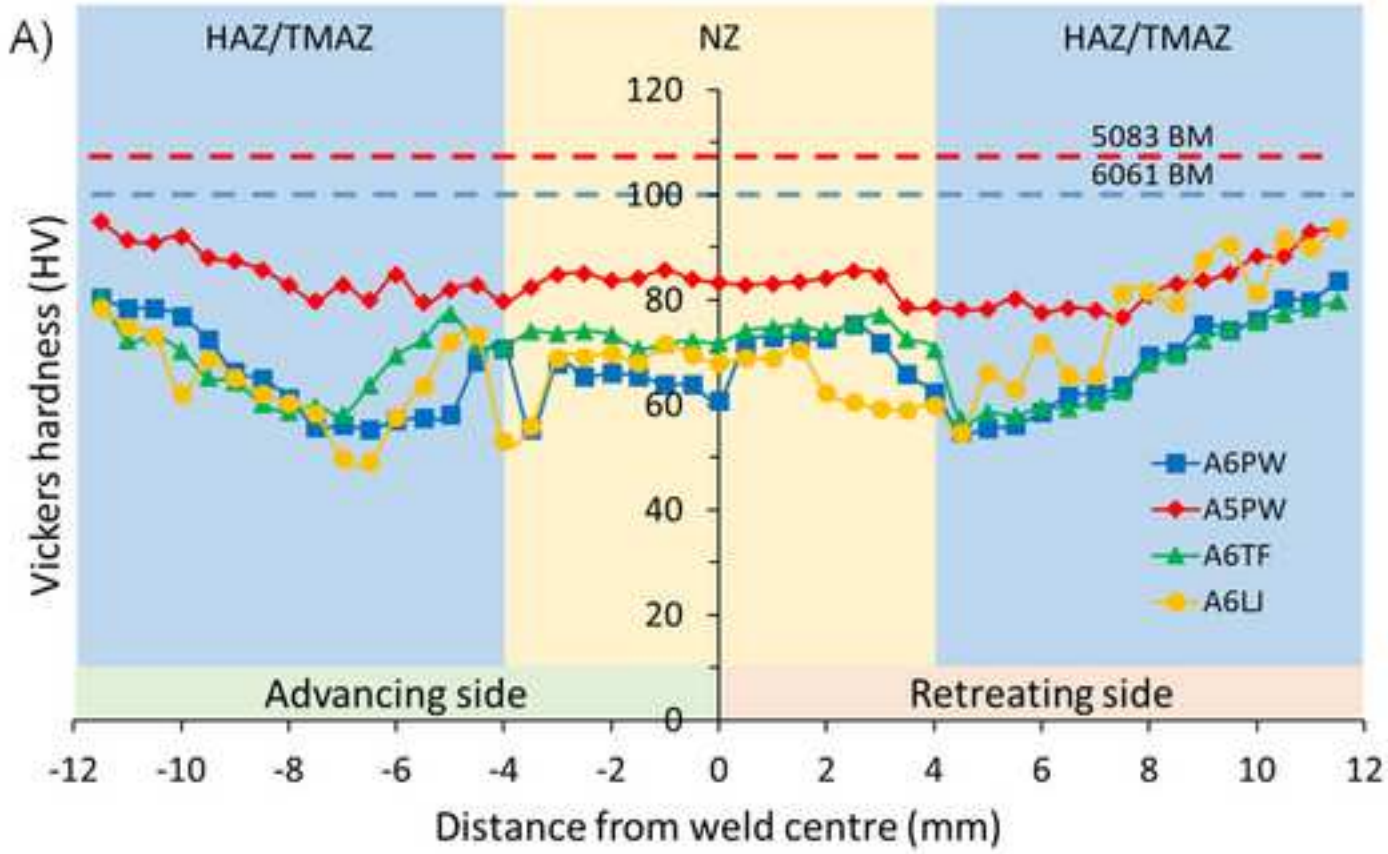

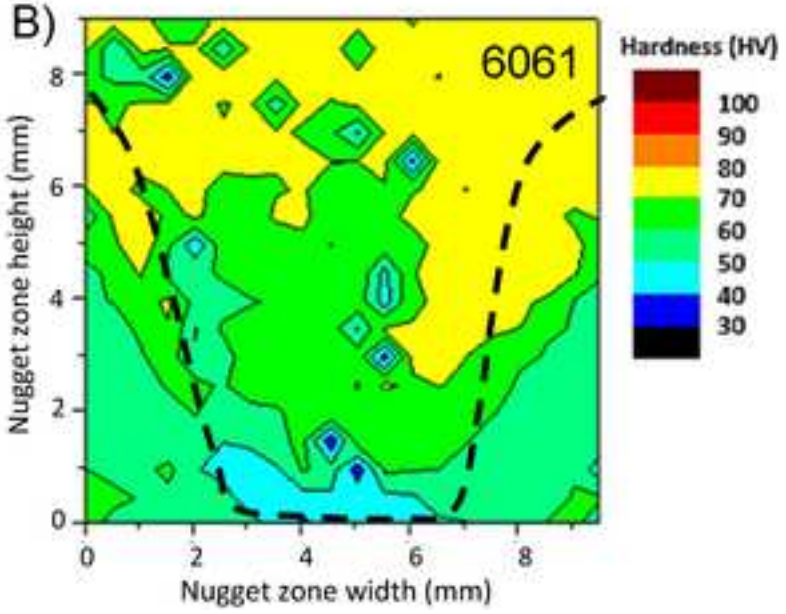

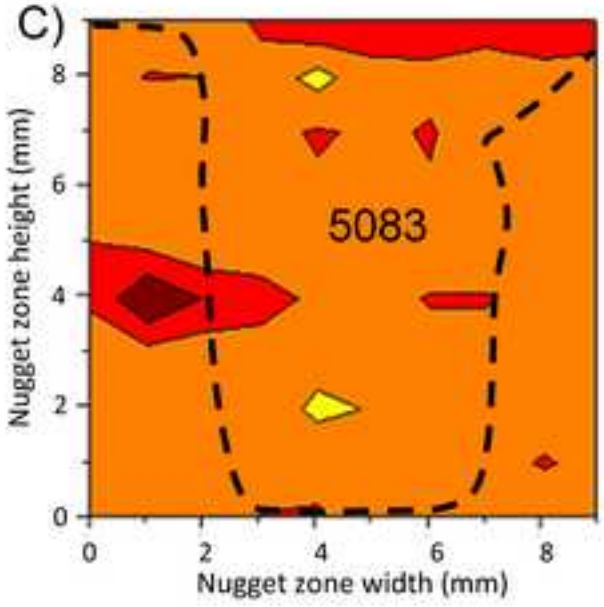

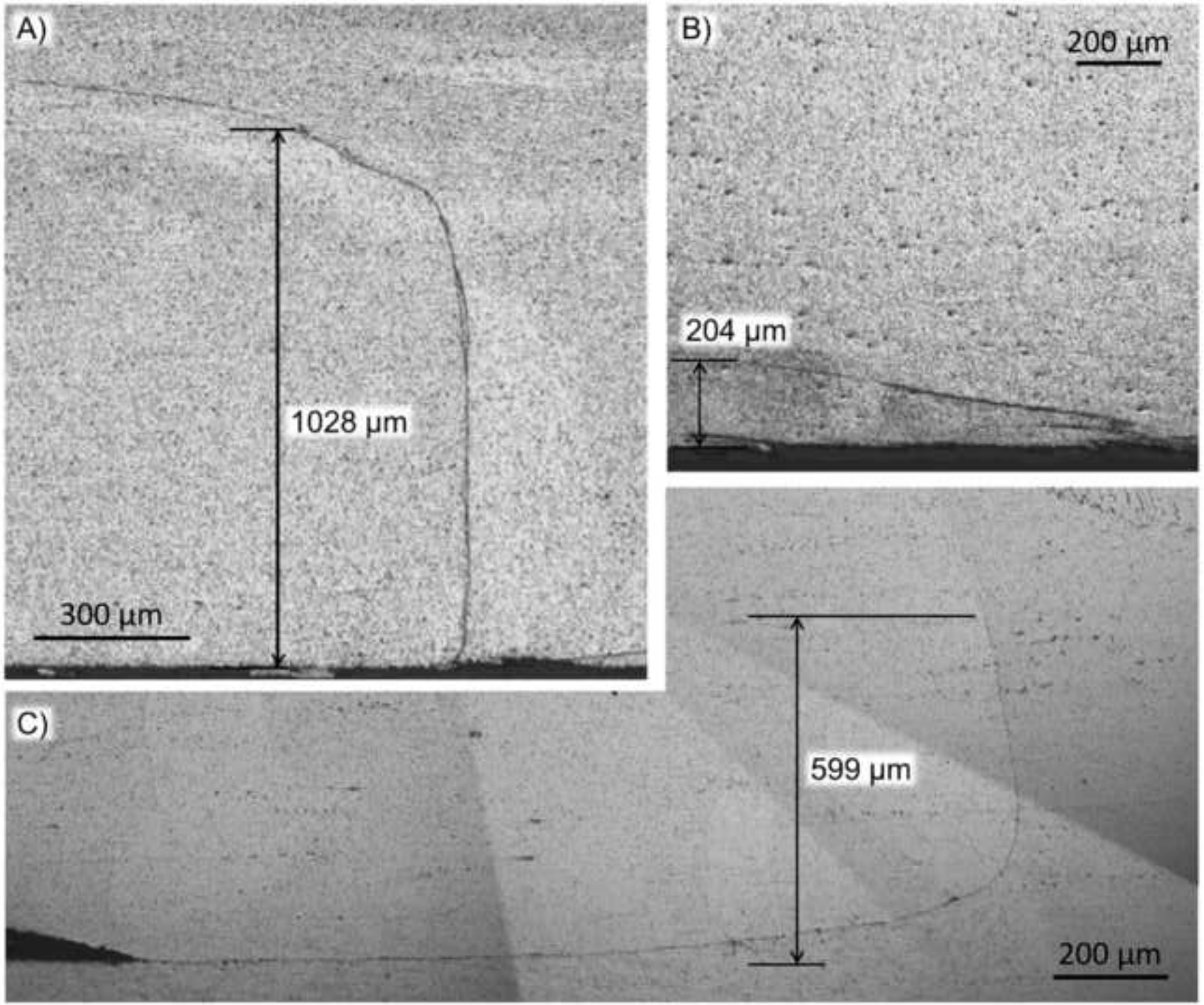

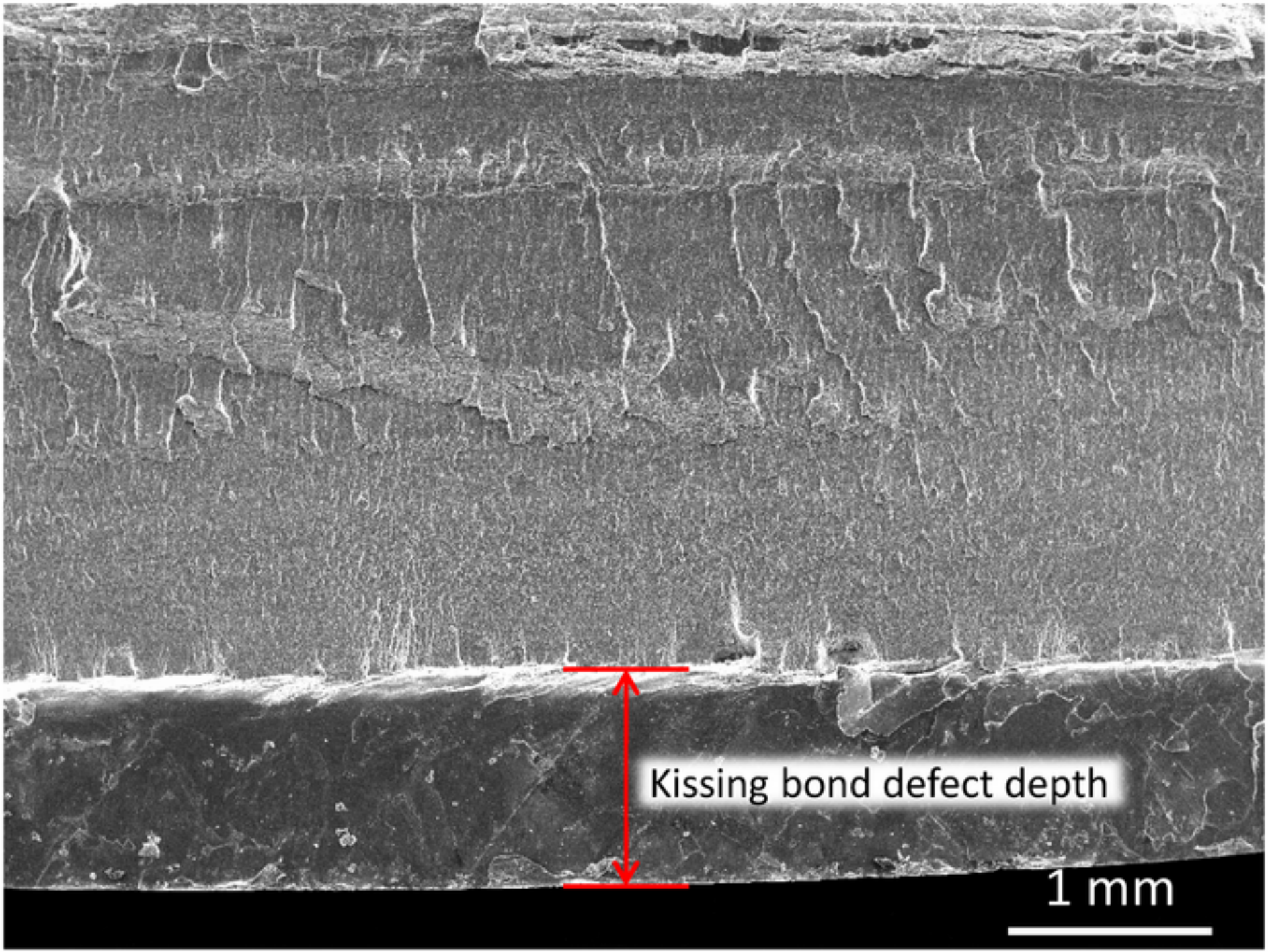

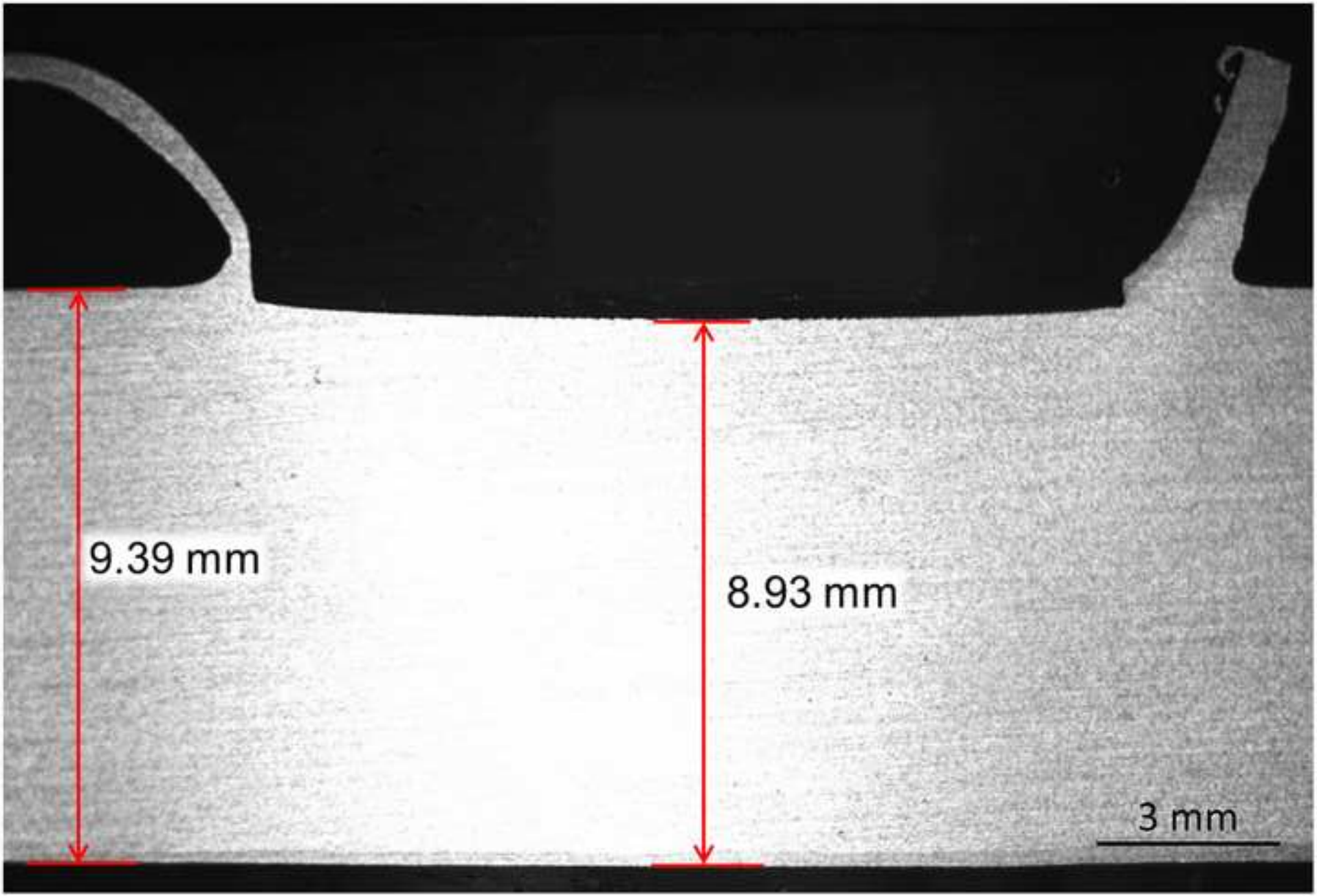

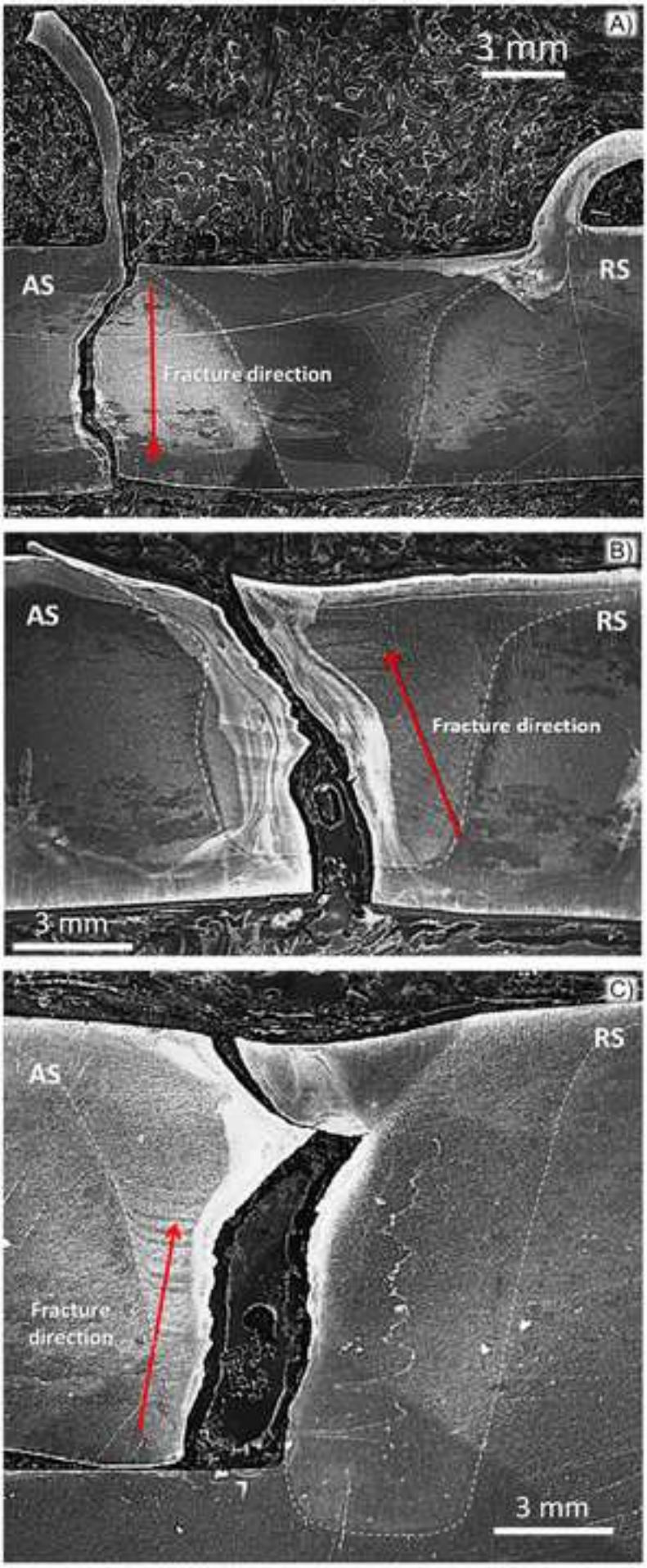

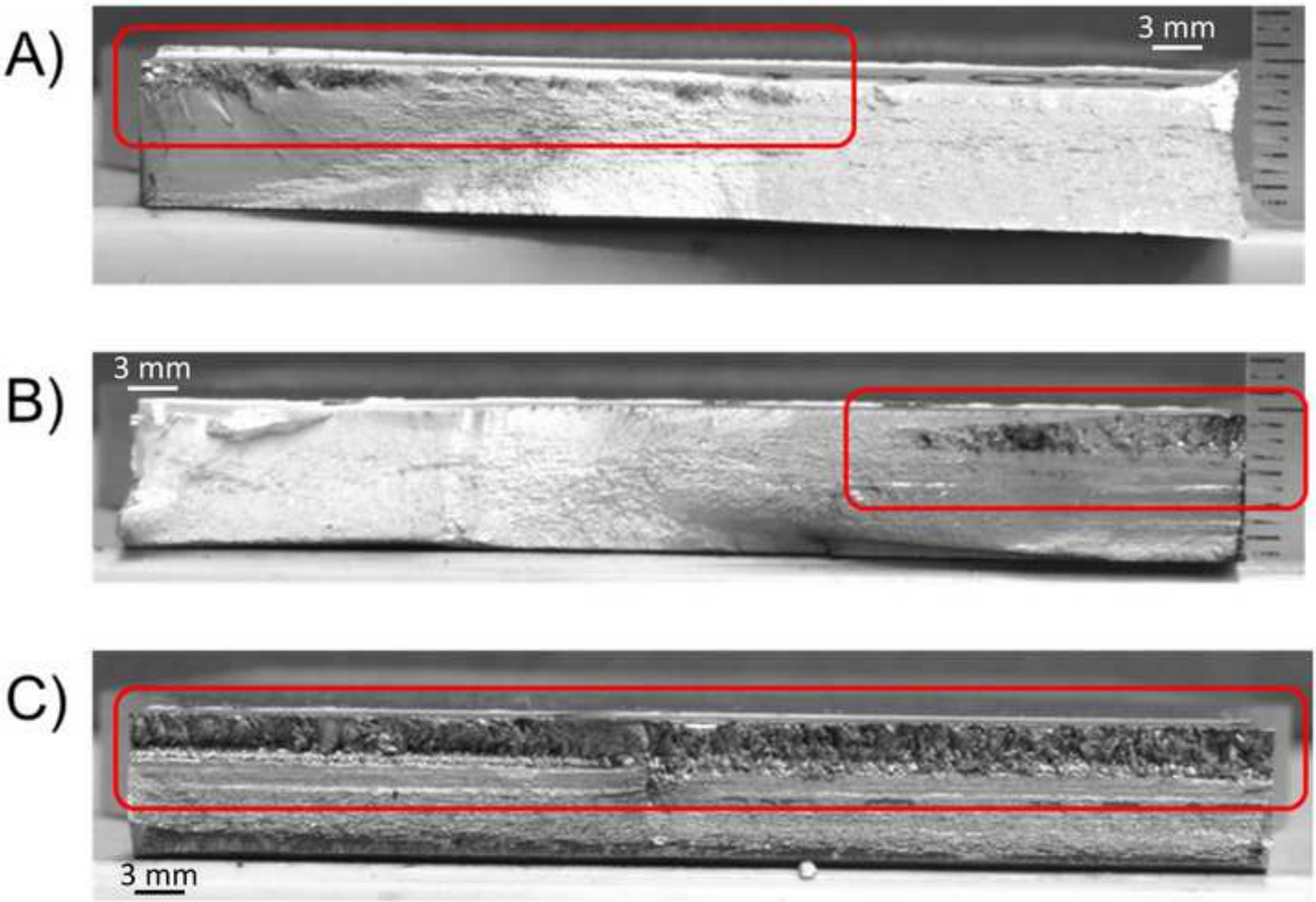

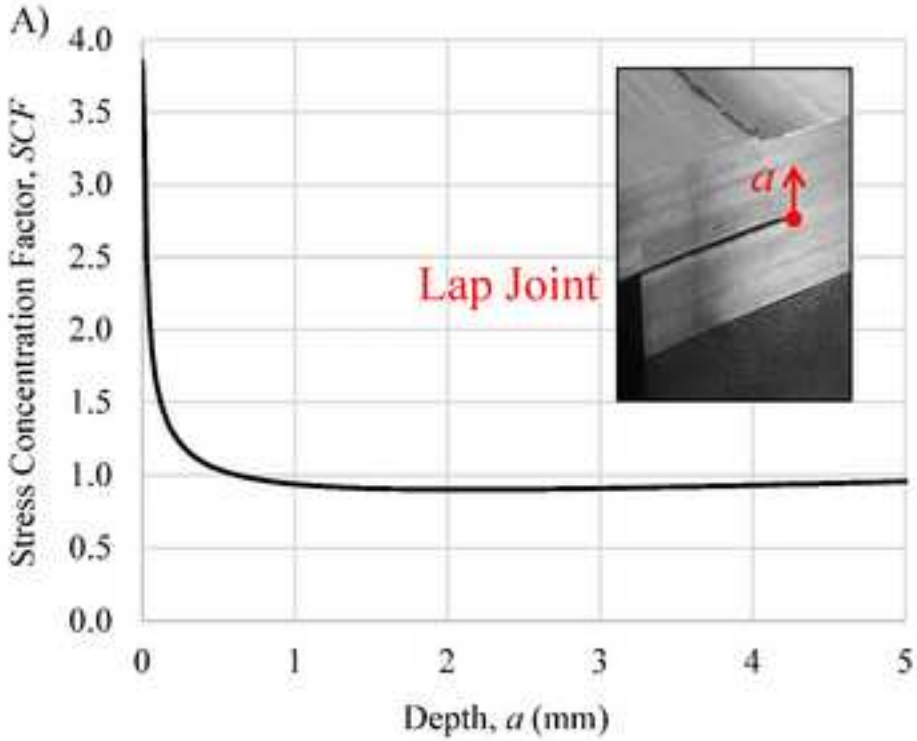

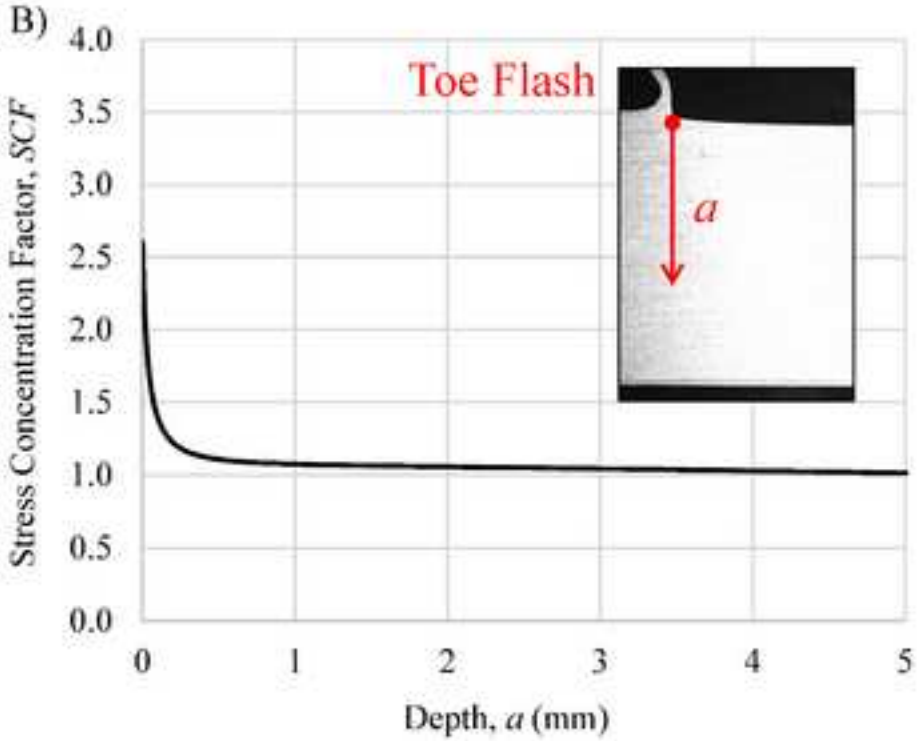

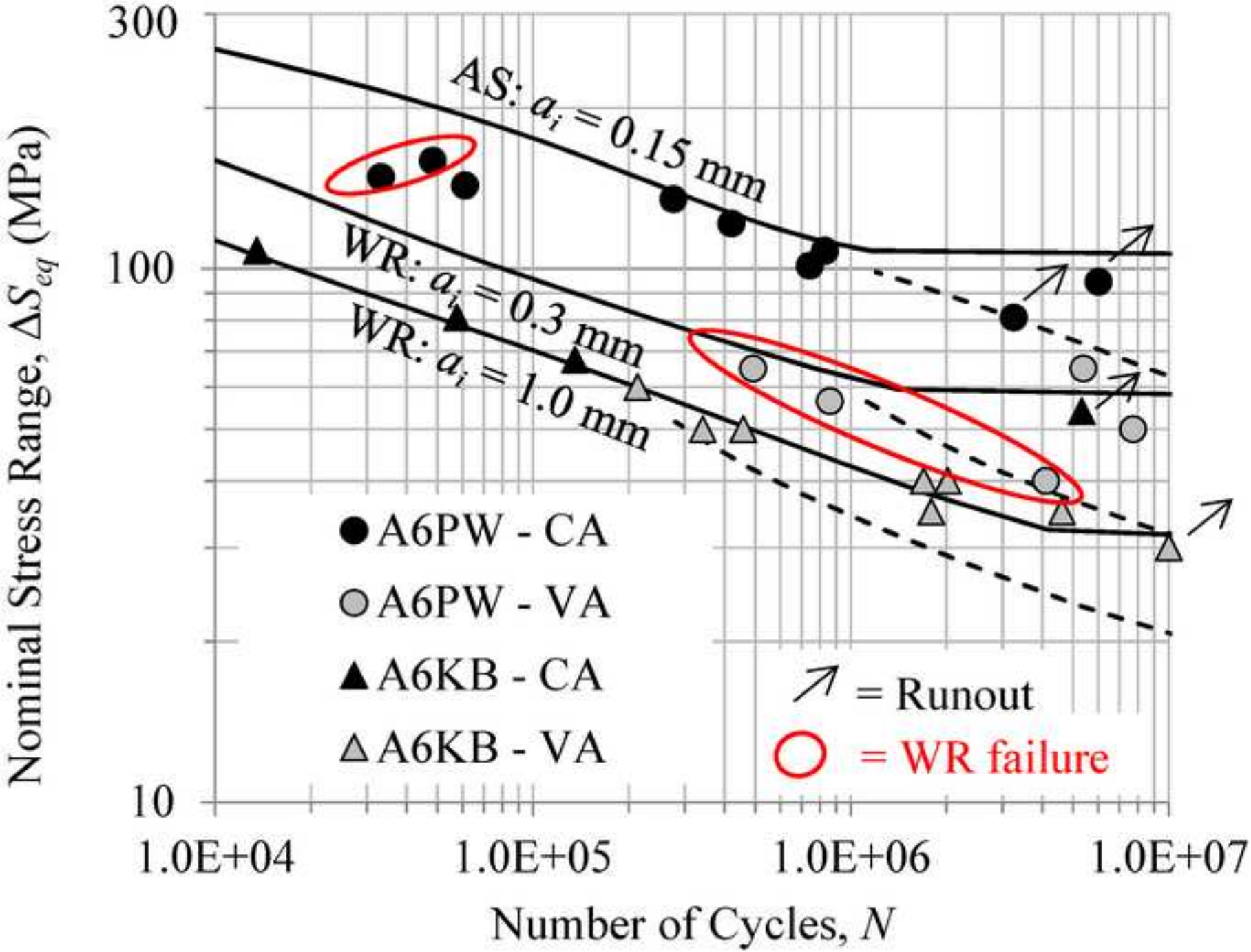

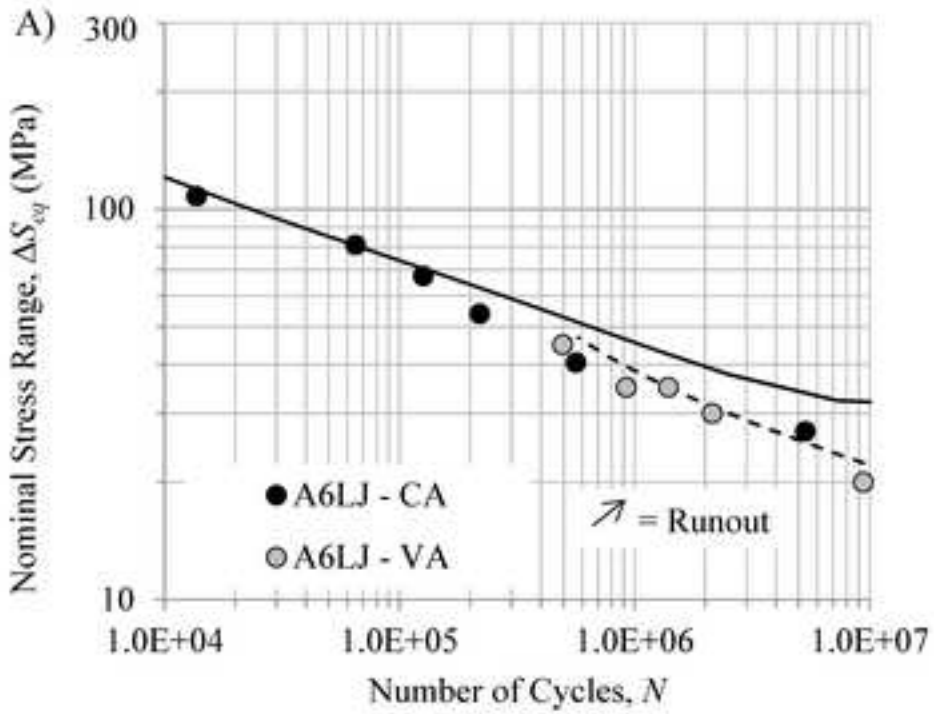

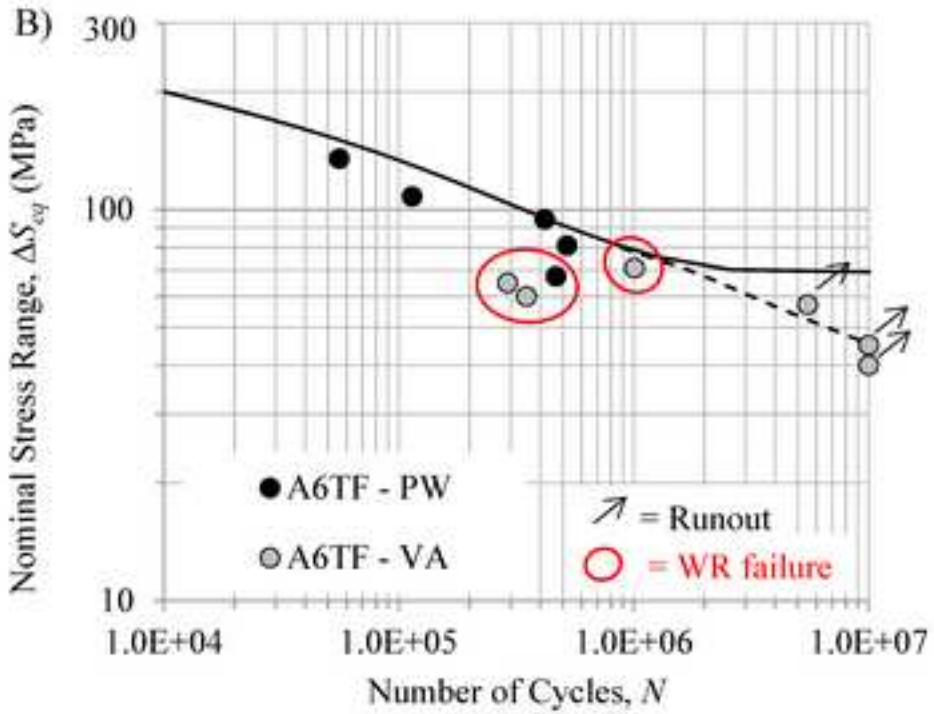

Graphical Abstract